Thermal Conductivity and Temperature Profiles in Carbon Electrodes for Supercapacitors

O.S. Burheim[a,b], Mesut Aslan[c], Jennifer S. Atchison[c], Volker Presser[c,d,*]

[a] *Dep. of Chemistry, NTNU - Norwegian University of Science and Technology, 7491 Trondheim, Norway.*

[b] *Dep. of Electrical and Computer Engin., HiST - Sør-Trøndelag University College, 7004 Trondheim, Norway.*

[c] *INM – Leibniz Institute for New Materials, Energy Materials Group, 66123 Saarbrücken, Germany.*

[d] *Dep. of Materials Science and Engin., Saarland University, 66123 Saarbrücken, Germany.*

Abstract

The thermal conductivity of supercapacitor film electrodes composed of activated carbon (AC), AC with 15 mass% multi-walled carbon nanotubes (MWCNTs), AC with 15 mass% onion-like carbon (OLC), and only OLC, all mixed with polymer binder (polytetrafluoroethylene), has been measured. This was done for dry electrodes and after the electrodes have been saturated with an organic electrolyte (1 M tetraethylammonium-tetrafluoroborate in acetonitrile, TEA-BF_4). The thermal conductivity data was implemented in a simple model of generation and transport of heat in a cylindrical cell supercapacitor systems. Dry electrodes showed a thermal conductivity in the range of 0.09 - 0.19 $WK^{-1}m^{-1}$ and the electrodes soaked with an organic electrolyte yielded values for the thermal conductivity between 0.42 - 0.47 $WK^{-1}m^{-1}$. It was seen that the values related strongly to the porosity of the carbon electrode materials. Modeling of the internal temperature profiles of a supercapacitor under conditions corresponding to extreme cycling demonstrated that only a moderate temperature gradient of several degrees Celsius can be expected and which depends on the ohmic resistance of the cell as well as the wetting of the electrode materials.

Keywords: Supercapacitor, Thermal Conductivity, Temperature Profiles

*Corresponding author. Tel: +49 681 9300 177. Fax: +49 681 9300 223.
Email address: volker.presser@inm-gmbh.de (Volker Presser)

1. Introduction

Electric double-layer capacitors (EDLC), more commonly known as supercapacitors or ultracapacitors, are devices capable of fast and energy-efficient energy storage. [1] Unlike batteries, where electrochemical reactions or ion insertion is utilized to transform electric energy, supercapacitors store energy exclusively *via* electrosorption of ions onto the surface of highly porous carbon electrodes [1]. They store energy exclusively via electrosorption of ions onto the surface of highly porous carbon electrodes, unlike batteries, where electrochemical reactions or ion insertion is utilized to transform electric energy [1]. As a result, EDLCs exhibit intrinsically high power density and moderate energy density, whereas batteries exhibit the opposite correlation; additionally, EDLCs enjoy long lifetime and up to 10^6 charge/discharge cycles [2]. Commercial EDLCs commonly use organic electrolytes coupled with composite film electrodes composed of porous carbon (usually activated carbon; 85-95 mass%), polymer binder (5-10 mass%), and additives to improve the electrical conductivity (*e.g.*, carbon black; ≈5 mass%) [3, 4]. In the past decade, a large array of carbon nanostructures (*e.g.*, carbon nanotubes, graphene, carbon onions), electrolytes (*e.g.*, aqueous / organic solvents, ionic liquids), and functional electrode designs (*e.g.* , thin films, printed electrodes, fiber mats) have been studied in detail with the goal of improving performance [5]. More specifically, many reviews have been published on electrode materials and electrolytes used in supercapacitors, [3, 5–8] best practice papers providing guidelines for electrochemical testing, [4, 9, 10] studies on the degradation and aging of supercapacitors, [11, 12] and perspectives elucidating current trends and future potentials of this technology [13–15].

Compared to electrical conductivity, the thermal conductivity of EDLC electrode materials and thermal device properties have received less attention. The active component of film electrodes is carbon, and the thermal conductivity of graphite [16], graphene [17], carbon nanotubes [18], among other carbon materials,

has been studied in great detail. From these studies, it is reasonable to assume a thermal conductivity in the range of 0.1-0.2 W m^{-1} K^{-1} for porous carbon, values reported for activated carbon measured in air [19]. These values are several orders of magnitude smaller than bulk carbon and graphite. Moreover, the thermal conductivity of porous materials can change significantly when adding liquids and applying compaction pressure. It is important to note that just a 10 K increase in temperature reduces the lifetime of an EDLC by a factor of two; therefore, a detailed knowledge of the thermal behavior of compressed porous electrodes with and without electrolytes is important when designing large scale EDLC systems [20].

For commercial applications it is common practice to model the thermal properties of a device in terms of the cell geometry. For instance, the temperature increase after one duty cycle of an EDLC device in a cylindrical cell can be described by a simple equation:

$$\Delta T = R_{\mathrm{thermal}} I^2 R_{\mathrm{el}} \tag{1}$$

where $R_{thermal}$ is the thermal resistance, I as the current, and R_{el} as the dc resistance (or the high frequency resistance in the case of ac currents). In order to use this equation correctly, R_{thermal} must be defined in the equation to describe: the geometry, the heat capacity of the device, and the cycle. Consequently, Eq. 1 is then also only valid for one cycle and not at stationary state with many repeated cycles. This equation also only applies to the *external* temperature profiles of supercapacitors. In order to asses also the *internal* temperature gradients the thermal conductivities reported in this paper is required. The small temperature increases experienced by EDLCs can be attributed to the highly efficient, non-faradaic physical charge storage mechanism. To assess the thermal behavior of an EDLC device, Virtanen et al. [21], monitored the temperature of the air used to cool a 64 F supercapacitor module. They measured an increase of 15°C when

the device was operated up to 300 W. For comparison, lithium ion batteries, [22] may exhibit a significant temperature increase that require elaborate thermal management solutions to ameliorate safety concerns due to destabilizing battery modules [23]. A more detailed temperature profile study was carried out by Gualous et al. [24] for a 316 F supercapacitor cell under constant 20 W power in-/output cycling, they reported the external temperature increased first by approximately 6 °C and then remained constant at around 34-35 °C with very small thermal fluctuations inside the supercapacitor ($\Delta T < 1$ °C). The same trend was also found at higher power and for 60 W a temperature increase of almost 60 °C was observed. This study illustrates that not only the operating voltage but the cycling conditions play a important role in the thermal behavior of the device, specially considering the flash point for acetonitrile is 82 °C very close to the observed temperature of the cycled device.

In this study, we investigate the thermal conductivity of film electrodes, composed of carbon and polymer binder, with and without electrolyte. In particular, we investigate to what extend the thermal properties of nanoscale carbon particles differs from micrometer-sized particles when processed into film electrodes, and how the electrolyte immersion affects the thermal properties.In addition to activated carbon, we have chosen carbon onions and multi-walled carbon nanotubes, which can be used as electrically conductive additives [25]. In addition to studying the thermal conductivity, we also provide model calculations on the thermal behavior of full cells in different geometries. The aim of this paper is to provide data that can ensure more detailed and more precise thermal engineering of supercapacitors.

2. Materials and Measurements

2.1. Thermal Conductivity Measurements

2.1.1. Apparatus

The apparatus used in the experiments is the same as the one reported in previous publications [26, 27] and is depicted in Fig. 1. In brief, we measure the heat passing through a sample and the temperature difference across the sample. This gives us the thermal resistance of the investigated sample, R_{sample}. The sample can be a stack of materials or a single layer. Here, we measure the sum of the sample- and the contact thermal resistance, R_{sample}+$2R_{\mathrm{contact}}$. We also measure the sample thickness, which by Fourier's first law allows us to obtain the thermal conductivity.

A heat flux is set up in two cylindrical pistons (sandwiching the investigated sample) by flowing water with fixed temperatures in the upper and lower part of the apparatus. This heat flux is measured in each part of the apparatus by three thermocouples (1-3 and 6-8 in Fig. 1). *Via* calibration (see [26]) we know the thermal conductivity of the stainless steel and, by Eqs. 2-3, the heat flux through the sample (accuracy ≈97%). A small aluminum cap with thermocouples is placed close to the end of the two pistons (4 and 5 in Fig. 1). Because of the high thermal conductivity aluminum, these caps are close to isothermal and, thus, act like extensions of the thermocouples. Therefore we can measure the temperature drop across the investigated sample and the quality of the contact to the piston. By using calibrated micrometer gauges, we measured the thickness with a precision of $\pm$ 3 μm.

$$q_{\mathrm{upper}} = k_{\mathrm{steel}} \frac{T_1 - T_3}{\delta_{1-3}} \quad \text{and} \quad q_{\mathrm{lower}} = k_{\mathrm{steel}} \frac{T_6 - T_8}{\delta_{6-8}} \tag{2}$$

$$q_{\text{sample}} = \frac{q_{\text{upper}} + q_{\text{lower}}}{2} \quad \text{and} \quad R_{\text{total}} = \frac{T_4 - T_5}{q_{\text{sample}}} \tag{3}$$

Figure 1

2.1.2. *Thermal Conductivity Measurements*

We chose both to stack the investigated material and to measure individual layers. We chose four combinations of cylindrical discs (Ø = 21 mm), so that we could vary the thickness in our measurements. Dry electrodes and electrodes wetted with aqueous or organic electrolyte were measured. We chose two types of electrolytes one organic and one aqueous. The organic electrolyte consisted of 1 M solution of tetraethylammonium tetrafluoroborat, TEA-BF_4, in acetonitrile (ACN). Measurements with the aqueous electrolyte are reported in Appendix A. The wetted electrodes were first cut into discs when dry and then stored in the electrolyte solution for approximately 24 h at room temperature. An exception was made for the electrode based on onion-like carbon (also called carbon onions), it was measured after having been stored for 24 h in the organic electrolyte and then measured again after having been stored in the organic electrolyte for 4 more days. When the wetted electrodes were put into the apparatus, some residual electrolyte was present at the surface of the disks in order to ensure complete wetting throughout the measurement.

2.1.3. *Statistical Analysis and Accuracy of the Measurements*

The thermal apparatus was calibrated using materials with known thermal conductivity, see Ref. [26]. These values are known with $\pm 5\%$ and therefore we can not report the thermal conductivity with better precision. The thermal conductivities in the result section reports deviations from the linear regression using a least square of residual approach. All numbers from the linear regressions are reported with 95% confidence intervals.

2.2. Electrode Materials

2.2.1. Electrode Preparation

For the preparation of electrode foils (Fig. 2), the following starting materials were used: (i) activated carbon, AC (YP-50F, Kuraray Chemicals, Japan), (ii) onion-like carbon, OLC (prepared by vacuum treatment of detonation nanodiamond purchased from NaBond Technologies Co. Ltd, China, at 1750 °C and 10^{-4} to 10^{-5} mbar for 3 h), and (iii) multi-walled carbon nanotubes, MWCNT (PlasmaChem, Germany). As active material, we used (a) pure AC, (b) AC with 15 mass% MWCNT, (c) AC with 15 mass% OLC, and (d) pure OLC. The mixtures of AC with either OLC or MWCNT were homogenized in dry state in a roll mixer prior to further treatment. For the preparation of electrodes from these materials, 5 mass% of polytetrafluoroethylene (PTFE, aqueous solution, Sigma Aldrich, Germany) was added; only in the case of pure OLC electrodes, 10 mass% of PTFE had to be added to obtain mechanically stable composite film electrodes. Using ethanol for dilution, a mortar and pestle was used to homogenise the PFTE/powder mixtures. Foils with a size of 30x30 mm^2 were prepared at room temperature by rolling the carbon/PTFE slurry with a twin roller at a speed of 25 mm s^{-1} (HR01 Hot Rolling Machine, MTI, Richmond, USA) resulting in a controlled thickness variation from 60-120 μm as shown in Appendix B. Finally, the electrode foils were dried in a vacuum oven at 150 °C and 100 mbar for 24 h (Memmert VO400, Germany).

2.2.2. Material Characteristization

Scanning electron microscopy (SEM) images were captured using a Quanta 400 ESEM (FEI, The Netherlands) in high vacuum mode at 15 kV. The samples were mounted on a conductive carbon stub, while for the analysis of cross-sections of the electrodes, we used a miniature bench sample holder. The samples were imaged uncoated and SEM micrographs can be seen in Fig. 2 and in Appendix B.

Table 1

Figure 2

2.3. Temperature Distribution Model

In order to give a perspective on the importance of the measured thermal conductivities we present a very simple thermal model. The model considers repeatedly charging and discharging cycles at constant current. Because the model considers continuous ampereostatic current within in any reasonable voltage window, the model becomes independent of the cell capacitance. The chosen modeling software applies a finite element method (FEM) and is COMSOL 4.2a. In this instance, COMSOL is set to solve Eq. 4 within every layer of the model. The model applies a quadratic (second order) mesh and was checked for mesh size dependency.

$$\nabla \left(k \nabla T \right) + \dot{P}_{\text{diss}} = 0 \tag{4}$$

where k is the thermal conductivity of that layer, T is the temperature, and $\dot{P}_{\text{diss}}$ is the power losses dissipated as heat per unit volume. In the presented simple model we consider only Joule type heating, which means that the heat, $\dot{P}_{\text{diss}}$, is equal to the squared current density, j^2, over the electric conductivity, κ. We consider the side surfaces to be insulating and that the outside surface to have a uniform fixed temperature (Dirichlet boundary condition). Thus we only investigate internal temperature profiles that come in addition to temperature gradients in cooling fluids surrounding the supercapacitor.

Moreover, the electric conductivity was based on observed cell resistance that was considered to be uniformly distributed across the cell thickness, see Table 2. We have chosen to use two values here in order to illustrate the impact of what expected cell resistivity, 0.1 and 1 Ω cm^2 [4, 28]. The values are chosen because they are realistic, differ by an order of magnitude and are in the higher end of what can be expected for commercial systems. The layers are furthermore considered to be in a repeating stack of current collector | electrode | separator | electrode | current collector | electrode and so on. The thermal conductivity values

applied are 200 W $K^{-1}m^{-1}$ for the current collector (aluminum) and 0.2 W $K^{-1}m^{-1}$ for the electrolyte. The chosen thermal conductivity for the electrolyte compartment is a little larger than for that of acetonitrile ($\approx$0.2 W $K^{-1}m^{-2}$ [29]). We justify this by assuming that the the salt and the separator (most polymers are ≈ 0.25 W $K^{-1}m^{-2}$) contributes to an increased value. Because the electrolyte compartment constitute only ten percent of the repeating cell thickness an an error in this assumption has a very small impact. The chosen current density is based on heavy cycling in the order of 1 ampere per gram of carbon and, with a density of approximately 0.5 g cm^{-3}, a total of 200 μm of electrode material per cell results in a current density of 10 mA cm^{-2}. The chosen geometry is based on a large commercial cylindrical design, 60 mm in diameter which is typical for commercial systems [30]. Table 2

3. Results and Discussion

3.1. Thermal Conductivity of the Electrode Material

Table 3

The thermal conductivity of the different electrode materials, dry and with residual electrolytes, are tabulated in Table 3. When the electrodes are dry, the thermal conductivity ranges from 0.09 to 0.19 W $K^{-1}m^{-1}$, and after immersion in the electrolyte, the thermal conductivity ranges from as low as 0.32 and up to 0.47 W $K^{-1}m^{-1}$.

The dry electrode material systems based on activated carbon (AC) all have close to the same thermal conductivity, whereas the electrode only composed of OLC and binder exhibits a somewhat lower thermal conductivity. While the difference is below 5%, it is at the threshold of the accuracy of the method; therefore, the rationale of nanoparticles showing a lower thermal conductivity compared to micrometer-sized particles is reasonable and corresponds with the electrode top view micrographs displayed in Fig. 2. One can see that the OLC electrode has a sponge like morphology. It consists of nanoparticles with a diameter

of approximately 5 nm, and can be the reason why the thermal conductivity of dry OLC is slightly smaller than that of AC. Furthermore, OLC displays the largest pore volume from gas sorption measurements; thus, the larger net amount of air or liquid (both with a thermal conductivity significantly smaller than pure carbon) will yield a smaller thermal conductivity of the film electrode. [31] Another reason for the difference in thermal conductivity may be the higher content of PTFE in the OLC electrode material. It has been observed that PTFE impedes the transport of heat in porous carbon structures [32–34]. Another important observation is that adding 15 mass% of MWCNTs or OLC, does not affect the thermal conductivity. Thus, one can conclude that the pore structure and the main bulk material constitute the most important factors for the electrode material effective thermal conductivity. This is also true for wet electrodes, although the addition of the electrolyte has a strong impact. That is, the electrolyte can increase the thermal conductivity by a factor between three or four, though the value of this factor depends on the porosity and bulk structure of the carbon material. All AC electrode material that were stored in the organic electrolyte have a thermal conductivity that does not deviate significantly from 0.46 W $K^{-1}m^{-1}$, whereas the OLC soaked in the electrolyte had a thermal conductivity of 0.32 W $K^{-1}m^{-1}$.

When measuring the thermal conductivity of a porous carbon material, the content and the structure of the inter particle pores is extremely important [27, 35]. For instance, water in a fibrous carbon paper can increase the thermal conductivity by as much as a factor of three. These observations are consistent with those seen in this study. Therefore, we measured and report here the thermal conductivity of the dry capacitor electrode and when soaked in an organic electrolyte. For the dry electrode, the heat is mainly conducted through contact points between each particle. As can be seen from the SEM micrographs, Fig. 2, the carbon particles are highly anisometric and have little contact surface between each other. When the electrolyte is present, the mesoscopic pores surrounding the particle-to-particle carbon contact points can be filled with electrolyte.

This is perhaps best realized when comparing the thermal conductivity of all the different materials involved. Carbon in itself can have thermal conductivity well above 100 and up to 1000 W $K^{-1}m^{-1}$, [36] whereas the thermal conductivity of air and acetonitrile are 0.025 and 0.20 W $K^{-1}m^{-1}$ [29, 37], respectively. Thus, liquid droplets replacing gas, and when creating thermal conducting bridges between the particles, can raise the effective thermal conductivity of the dry bulk electrode material by several orders.

3.2. Effect of Electrode Compaction Pressure

In the presented results, the thermal conductivity is reported for a compaction pressure of 9.2 bar. We have three important reasons for discussing impact of the pressure; one is the verification of our choice to present the thermal conductivity values at only one pressure, a second reason is related to the validity of reusing the OLC-based electrode material after having exposed this to several compaction pressures, and a third reason is to compare the compression sensitivity of some material properties of supercapacitor electrodes to those of other electrochemical electrodes and systems.

The total measured thermal resistance, R_{total} in Eq. 3, is plotted for three different compaction pressures in Fig. 3. The different pressures are presented within the same window, so that one can see that the slopes does not change with the compaction pressure. The lower compaction shows a somewhat higher scatter, which is typical for this specific apparatus. Because the slope is constant with pressure and since the thermal conductivity equals the inverse value of the slope, we conclude that the thermal conductivity of the bulk electrode material is constant with compaction pressure. Looking at the data points of the graphs in Fig. 3 and 4, one can see that also the thickness is constant with pressure. Figure 4 shows the electrode thicknesses during a compression cycle up to around 16 bar and down again . We show this here in a separate figure in order to emphasize that the electrodes are not compressible within the pressure range and the precision of the apparatus. In fact, double standard deviations of $\pm$ 3-5 μm is very small for this type of measurements.

Mathematically, there is no significant differences between any of the measured thicknesses. Many other porous materials used for electrochemical energy converters and accumulators are compressible and the thermal conductivity then also relies heavily on the level of compression. It is in this light that the reported thickness-pressure dependency and the effective thermal conductivity as a function of compaction pressure is important knowledge also beyond the subject of supercapacitors.

Neither the electrode material thickness, nor the thermal conductivity changed with applied compaction pressure in our experiments. The constant thickness and the constant thermal conductivity can be seen as a related effect: after calendaring of the film electrodes, the bulk material has become so rigid that thermal contact between the carbon particles does not change and thus the thermal conductivity remains constant. This observation justifies presenting all the thermal conductivities at only one compaction pressure. For comparison, a recent study of dry compressible microporous materials consisting of activated carbon and 10-25 mass% PTFE showed that at maximum compression the thermal conductivity is, like in this study, around 0.10-0.13 W $K^{-1}m^{-1}$ [38].

Figure 3

Figure 4

Figure 5

3.3. Modeling of Internal Temperature Profiles

As described in Section 2.3, we apply a simple thermal model for two supercapacitor configurations. This model is made primarily to illustrate potential internal temperature gradients of the measured thermal conductivities. Because laboratory made supercapacitor cells can have much larger electric resistance than commercially prepared supercapacitors, we have chosen to model internal temperature profiles with two different resistances that differ by one order in magnitude, (*i.e.*, 0.1 and 1 Ohm cm^2) in order to provide a basis for comparison for well-optimized systems and custom made laboratory cells. The low resistance is considered being representative for a commercially prepared supercapacitor and the high resistance is considered being potentially representative for the less well prepared in-house prepared supercapacitors.

The modeled temperature profiles from the center and to the surface for the cylindrical cells are shown in Fig. 5. The models considers the thermal conductivity values obtained for the dry AC, the OLC with residual organic electrolyte, and the activated carbon with residual organic electrolyte, which are 0.13, 0.32, and 0.46 W $K^{-1}m^{-1}$, respectively. The upper left temperature profiles in Fig. 5 (A) show the modeled temperature profiles for the cylindrical the high ohmic resistance (1 Ω cm^2) and panel (B) shows the temperature profiles for the models with the low electrical resistance (0.1 Ω cm^2). The electrical resistance differs by one order of magnitude; so does also the range on the y-axes (vertical), and, thus, the temperature profiles appear to be the same. This demonstrates the linear coupling of the heat sources as indicated in both Eq. 1 and 4. Thus one can extrapolate the predicted temperature profiles to any given cell resistance.

Although the thermal conductivities are almost to linear (0.13, 0.32 and 0.46 W $K^{-1}m^{-1}$), the temperature profiles are not. This suggests that there is a limit to how small the internal temperature profiles can be. In supercapacitors, one will never encounter completely dry electrodes, though a small leakage of electrolyte could in theory lead to a lowered thermal conductivity and correspodingly increased temperature profiles. The graphs for the dry electrodes are shown here to illustrate the maximum temperature profiles possible. Another point to be mentioned in this discussion is that these temperature increments are in addition to those in the cooling air. When flowing air around heated cylinders, the surfaces of the cylinders can easily be several degrees ($\sim$10 °C) higher than the bulk air stream, because of the fluid boundary layer [22]. Thus, when summarizing the air temperature increase of air into and out of a supercapacitor system, the boundary layer temperature increase, and the internal temperature increment (as seen in Fig. 5) one can gain an overview of the maximum temperature of the supercapacitor system in operation relative to the ambient temperature. Despite very low thermal conductivities, the internal temperature differences appear to be smaller than the ambient temperature differences next to the surface encapsulating the supercapacitor.

4. Conclusions

We have measured the thermal conductivity of four combinations of supercapacitor electrode materials both dry and in combination with an electrolytes. The dry materials were found to have thermal conductivities in the range of 0.09 - 0.19 W $K^{-1}m^{-1}$ and the electrodes in contact with electrolyte had a thermal conductivity ranging from 0.42 to 0.47 W $K^{-1}m^{-1}$.

The observation of a lower thermal conductivity for OLC, consistently for dry and wet electrodes, strongly implies that a high net pore volume is detrimental to conduction of heat; clearly, this aspect needs to be taken into account when designing electrodes from materials with a very high pore volume or low packing density (*e.g.*, nanofiber electrodes).

Modeling supercapacitor internal temperature profiles under conditions corresponding to extreme cycling and a commercially sized unit demonstrated that temperature gradient of several degrees can be expected and that this depends on the ohmic resistance of the cell and on the wetting of the electrode materials. Compared to the external temperature difference measured in cooling fluids, the internal ones are of a second ranked size.

Acknowledgement

The Norwegian Research Council is acknowledged for financial support, FRIENERGI, grant number 197598 and the RENERGI, grant number 164466/S30.

The authors thank Prof. Eduard Arzt for his continuing support. MA, JSA, and VP acknowledge funding from the German Federal Ministry for Research and Education (BMBF) in support of the nanoEES^{3D} project (award number 03EK3013) as part of the strategic funding initiative energy storage framework.

References

[1] A. Pandolfo, A. Hollenkamp, Carbon properties and their role in supercapacitors, J. Power Sources 157 (2006) 11 – 27.

[2] J. Miller, P. Simon, Fundamentals of electrochemical capacitor design and operation, Electrochem. Soc. Interf. 17 (2008) 31–32.

[3] E. Frackowiak, F. Béguin, Carbon materials for the electrochemical storage of energy in capacitors, Carbon 39 (2001) 937–950.

[4] A. Burke, M. Miller, Testing of electrochemical capacitors: Capacitance, resistance, energy density, and power capability, Electrochimica Acta 55 (2010) 7538–7548.

[5] P. Simon, Y. Gogotsi, Materials for electrochemical capacitors, Nature Mat. 7 (2008) 845–854.

[6] L. Zhang, X. Zhao, Carbon-based materials as supercapacitor electrodes, Chem. Soc. Reviews 38 (2009) 2520–2531.

[7] M. Inagaki, H. Konno, O. Tanaike, Carbon materials for electrochemical capacitors, J. Power Sources 195 (2010) 7880–7903.

[8] F. Béguin, E. Frackowiak, Carbons for Electrochemical Energy Storage and Conversion Systems, Boca Raton: CRC Press, 2009.

[9] M. Stoller, R. Ruoff, Best practice methods for determining an electrode material's performance for ultracapacitors, Energy Environ. Sci. 3 (2010) 1294–1301.

[10] Y. Gogotsi, P. Simon, True performance metrics in electrochemical energy storage, Sci. 334 (2011) 917–918.

[11] P. Azais, L. Duclaux, P. Florian, D. Massiot, M.-A. Lillo-Rodenas, A. Linares-Solano, J.-P. Peres, C. Jehoulet, F. Béguin, Causes of supercapacitors ageing in organic electrolyte, J. Power Sources 171 (2007) 1046–1053.

[12] P. Ruch, D. Cericola, A. Foelske-Schmitz, R. Kötz, A. Wokaun, Aging of electrochemical double layer capacitors with acetonitrile-based electrolyte at elevated voltages, Electrochimica Acta 55 (2010) 4412–4420.

[13] A. Burke, Ultracapacitors: why, how, and where is the technology, J. Power Sources 91 (2000) 37–50.

[14] J. Miller, A. Burke, Electrochemical capacitors: Challenges and opportunities for real-world applications, Electrochem. Soc. Interf. 17 (2008) 53–57.

[15] J. Miller, Valuing reversible energy storage, Sci. 335 (2012) 1312–1313.

[16] P. Klemens, D. Pedraza, Thermal conductivity of graphite in the basal plane, Carbon 32 (1994) 735–741.

[17] A. Balandin, S. Ghosh, W. Bao, I. Calizo, D. Teweldebrhan, F. Miao, C. Lau, Superior thermal conductivity of single-layer graphene, Nano Lett. 8 (2008) 902–907.

[18] J. Che, T. Çağin, W. Goddard III, Thermal conductivity of carbon nanotubes, Nanotechnology 11 (2000) 65–69.

[19] G. Cacciola, G. Restuccia, L. Mercadante, Composites of activated carbon for refrigeration adsorption machines, Carbon 33 (1995) 1205–1210.

[20] H. Gualous, R. Gallay, Supercapacitor Module Sizing and Heat Management under Electric, Thermal, and Aging Constraints, WILEY-VCH Verlag GmbH & Co. KGaA, 2013, Ch. 11, pp. 373–476.

[21] A. Virtanen, H. Haapala, S. Hannikainen, T. Muhonen, H. Tuusa, Calorimetric efficiency measurements of supercapacitors and lithium-ion batteries, Conference Proceedings - IEEE Applied Power Electronics Conference and Exposition - APEC (2011) 1367–1373.

[22] T. Bandhauer, S. Garimella, T. Fuller, A critical review of thermal issues in lithium-ion batteries, J. Electrochem. Soc. 158 (2011) R1–R25.

[23] D. H. Doughty, P. C. Butler, R. G. Jungst, E. Roth, Lithium battery thermal models, J. Power Sources 110 (2002) 357–363.

[24] H. Gualous, H. Louahlia, R. Gallay, Supercapacitor characterization and thermal modelling with reversible and irreversible heat effect, IEEE Trans. Power Electronics 26 (2011) 3402–3409.

[25] W. Pabst, E. Gregorová, Mooney-type relation for the porosity dependence of the effective tensile modulus of ceramics, J. Mat. Sci. 39 (2004) 3213–3215.

[26] O. Burheim, P. Vie, J. Pharoah, S. Kjelstrup, *Ex-situ* measurements of through-plane thermal conductivities in a polymer electrolyte fuel cell, J. Power Sources 195 (2010) 249–256.

[27] O. S. Burheim, G. Ellila, J. D. Fairweather, A. Labouriau, S. Kjelstrup, J. G. Pharoah, Ageing and thermal conductivity of porous transport layers used for pem fuel cells, J. Power Sources 221 (2013) 356–365.

[28] Y. Gao, V. Presser, L. Zhang, J. J. Niu, J. K. McDonough, C. R. Pérez, H. Lin, H. Fong, Y. Gogotsi, High power supercapacitor electrodes based on flexible tic-cdc nano-felts, J. Power Sources 201 (0) (2012) 368 – 375.

[29] G. Cai, H. Zong, Q. Yu, R. Lin, Thermal conductivity of alcohols with acetonitrile and n,n-dimethylformamide, J. Chem. Eng. Data 38 (1993) 332–335.

335 [30] Maxwell, Data sheet - k2 series ultracapacitors - mod: Bcap3000 p270 k04/05 (February, 2013) 1–4.

336 [31] Z. Zivcova, E. Gregorova, W. Pabst, D. Smith, A. Michot, C. Poulier, J. European Ceram. Soc. 29
337 (2009) 347–353.

338 [32] M. Khandelwal, M. Mench, Direct measurement of through-plane thermal conductivity and contact
339 resistance in fuel cell materials, J. Power Sources 161 (2006) 1106–1115.

340 [33] E. Sadeghi, N. Djilali, M. Bahrami, Effective thermal conductivity and thermal contact resistance of
341 gas diffusion layers in proton exchange membrane fuel cells. part 1: Effect of compressive load, J.
342 Power Sources 196 (2011) 246–254.

343 [34] O. Burheim, H. Lampert, J. Pharoah, P. Vie, S. Kjelstrup, Through-plane thermal conductivity of
344 PEMFC porous transport layers, ASME J. of Fuel Cell Sci. & Technology 8 (2011) 021013–1–11.

345 [35] Y. Wang, M. Gundevia, Measurement of thermal conductivity and heat pipe effect in hydrophilic and
346 hydrophobic carbon papers, Int. J. Heat and Mass Transfer 60 (2013) 134–142.

347 [36] F. Robinson, J. G. Cevallos, A. Bar-Cohen, H. Bruck, Modeling and validation of a proto-
348 type thermally-enhanced polymer heat exchanger, ASME 2011 2011 Int. Mech. Engin. Exposition
349 IMECE2011-65684 (2011) 1–10.

350 [37] R. C. West, CRC - Handbook of physical and chemical properties, 58th Edition, CRC press, Inc.,
351 1977-1978.

352 [38] O. S. Burheim, H. Su, S. Pasupathi, J. G. Pharoah, B. G. Pollet, Thermal conductivity and temper-
353 ature profiles of the micro porous layers used for the polymer electrolyte membrane fuel cell, Int. J.
354 Hydrogen Energy in-press (2013) http://dx.doi.org/10.1016/ j.ijhydene.2013.04.140.

Appendix A. Thermal Conductivity in Presence of an Aqueous Electrolyte

The electrodes based on AC, AC+15 mass% OLC, and AC+15 mass% MWCNT were soaked in an aqueous electrolyte (1 M Na_2SO_4 in deionized water) for 24 hours. The interaction between water and the electrodes led to the electrodes expanding and partly disintegrating. It was also found difficult to obtain consistent results for the thermal conductivity. The values vary from 0.19 and up to 0.56 W K^{-1} m^{-1} and are tabulated in Table A.4.

When we look at the thermal conductivity of the AC-based electrode materials in combination with the aqueous electrolyte, the reported thermal conductivity values are scattered. A likely reason for the scatter on the measurement with the aqueous electrolyte present is that the PTFE from the manufacturing process is making it difficult to reproducibly and uniformly wet the electrode material. The PTFE is first dispersed in water, next mixed with carbon particles, then dried, heated, and calendered. This procedure creates an electrode material that is not reproducibly wetted by water. The lack of good wettability is similar to experience with other PTFE treated porous carbon materials in combination with water. [27, 34] We report on this material here not because we wish to predict an exact thermal conductivity value and corresponding possible temperature profiles, but because we wish to highlight the variety of the possible thermal conductivity of this material. The fact that the value varies from being almost as low as for the dry material and even larger than for the AC in the organic electrolyte suggests that temperature profiles during cycling are within the same range those of capacitors in dry and organic wetted electrodes.

Table A.4

Appendix B. Material Overview

The electrode material cross sectional thickness and macro-porous structure can be seen in Fig. B.6.

Figure B.6

Tables

Table 1: Particle size, specific surface area (SSA), volume-weighted average pore size, and total pore volume for the used carbon film electrode materials.

Property	AC	OLC	MWCNT	AC + MWCNT[a]	AC + OLC[a]
Particle size / μm	5-20	0.005-0.01	1-10[b]	1-20	0.005-20
BET SSA[c] / m^2g^{-1}	1730	371	213	1500	1508
DFT SSA[d] / m^2g^{-1}	1530	383	211	1338	1343
Average pore size[e] / nm	0.94	13.8	14.0	1.05	1.10
Total pore volume[d] / cm^3g^{-1}	0.74	1.26	0.54	0.73	0.79

[a]85 mass% AC. [b]Particle size = length of the multi-walled carbon nanotube. [c]Calculated in the linear regime in the relative pressure range from 0.05 to 0.20 P/P_0. [d]Calculated using quenched-solid density functional theory (QSDFT) and assuming slit-shaped pores. [e]Average pore size = volume-weighted pore size average calculated *via* $\frac{\sum_{i=1}^{n} d_i V_i}{\sum_{i=1}^{n} V_i}$, with d as the pore width and V as the pore volume

Table 2: Overview on the properties of the thermal models.

Cylindrical cell	h=0.100 m	d=0.036 m
$\delta_{\text{electrolyte}}$	$\delta_{\text{current collector}}$	$\delta_{\text{electrode}}$
25 μm	25 μm	100 μm
R_{cell}	κ_{mean}	j_{mean}
0.1 Ω cm^2	0.25 S cm^{-1}	
1 Ω cm^2	0.025 S cm^{-1}	0.010 A cm^{-2}

Table 3: Overview of measured thermal conductivities for the electrodes when dry and when soaked in the electrolyte (1M TEA-BF_4 in acetonitrile).

Sample	Dry	With electrolyte
Activated carbon (AC)	0.13±0.01	0.47±0.04
AC + 15 mass% MWCNT	0.14±0.05	0.46±0.01
AC + 15 mass% OLC	0.13±0.04	0.44±0.02
Onion-like carbon	0.10±0.01	0.32±0.01

Table A.4: Measured thermal conductivity for the electrode materials soaked in the aqueous electrolyte.

Material	k / W K^{-1} m^{-1}
AC	0.28±0.09
AC + 15 mass% MWCNT	0.55±0.01
AC + 15 mass% OLC	0.32±0.03

Figure Captions

Figure 1. A sketch of the thermal conductivity meter used for our study (cf. Ref. [26, 27]).

Figure 2. SEM micrographs of (A) activated carbon (AC), (B) AC and 15 mass% multi-walled carbon nanotubes (MWCNTs), (C) AC and 15 mass% onion-like carbon (OLC), and (D) OLC. Samples A, B, and C contained 5 mass% polymer binder (polytetrafluoroethylene, (PTFE)) and D contained 10 mas% of PTFE.

Figure 3. Measured total thermal resistance of dry electrodes at 4.6 (brown), 9.2 (red), and 13.8 (blue) bar compaction pressure.

Figure 4. Measured thickness as a function of compaction pressure when increasing the pressure (black line and error bars) and when lowering (red line and error bars) the compression of the sample.

Figure 5. Modeled temperature profiles of the cylindrical cell with the 1 Ohm cm^2 (A) and the 0.1 Ohm cm^2 (B) cell resistance.

Figure B.6. Scanning electron microscopy (SEM) cross-sectional micrographs of the electrodes.

Figures

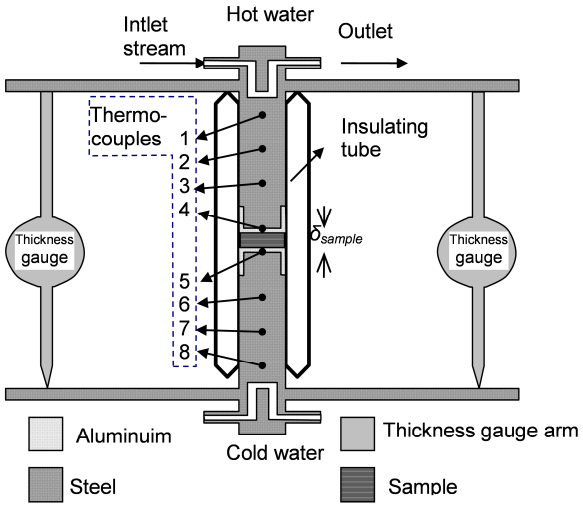

Figure 1: A sketch of the thermal conductivity meter used for our study (cf. Ref. [26, 27]).

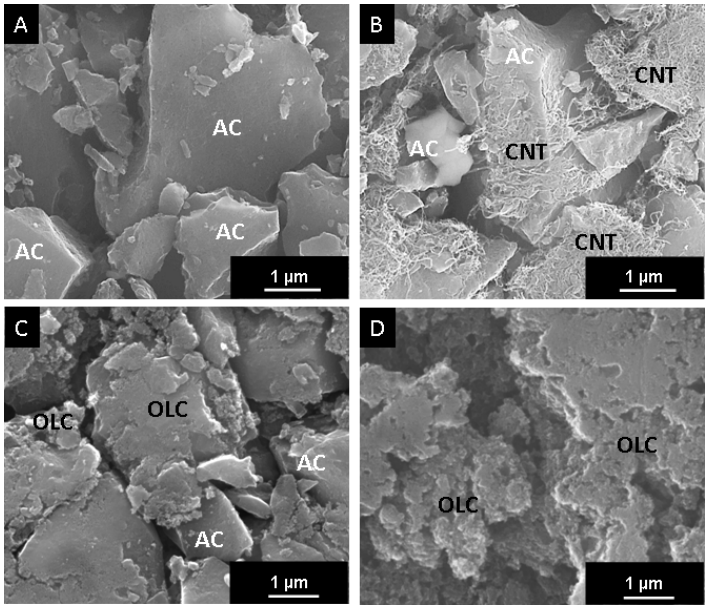

Figure 2: SEM micrographs of (A) activated carbon (AC), (B) AC and 15 mass% multi-walled carbon nanotubes (MWCNTs), (C) AC and 15 mass% onion-like carbon (OLC), and (D) OLC. Samples A, B, and C contained 5 mass% polymer binder (polytetrafluoroethylene, (PTFE)) and D contained 10 mas% of PTFE.

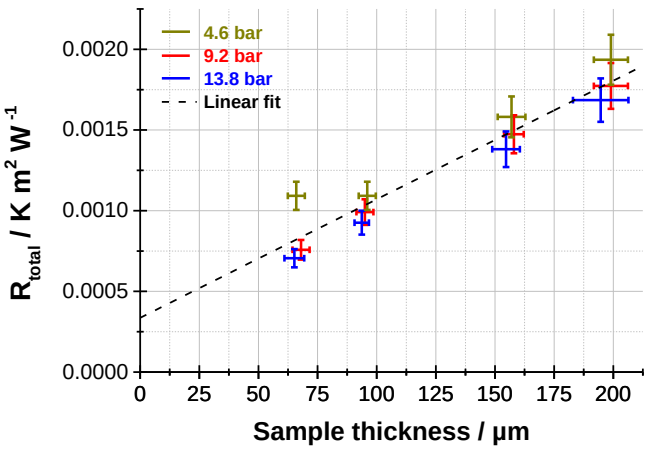

Figure 3: Measured total thermal resistance of dry electrodes at 4.6 (brown), 9.2 (red), and 13.8 (blue) bar compaction pressure.

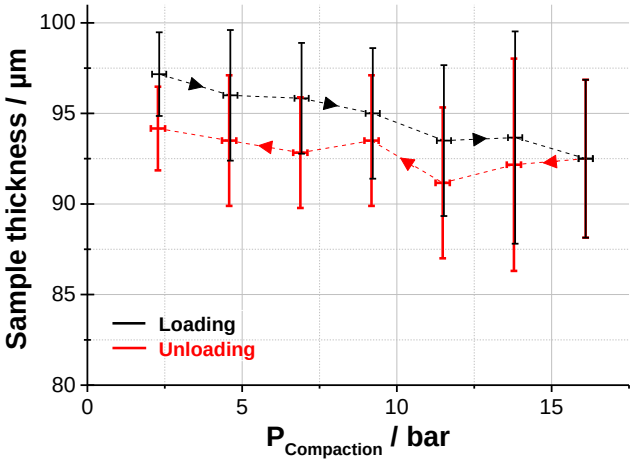

Figure 4: Measured thickness as a function of compaction pressure when increasing the pressure (black line and error bars) and when lowering (red line and error bars) the compression of the sample.

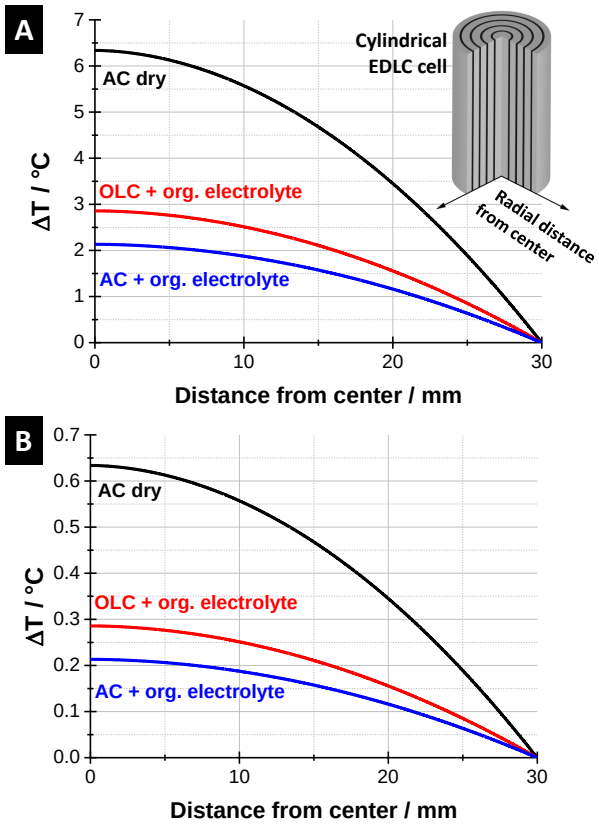

Figure 5: Modeled temperature profiles of the cylindrical cell with the 1 Ohm cm^2 (A) and the 0.1 Ohm cm^2 (B) cell resistance.

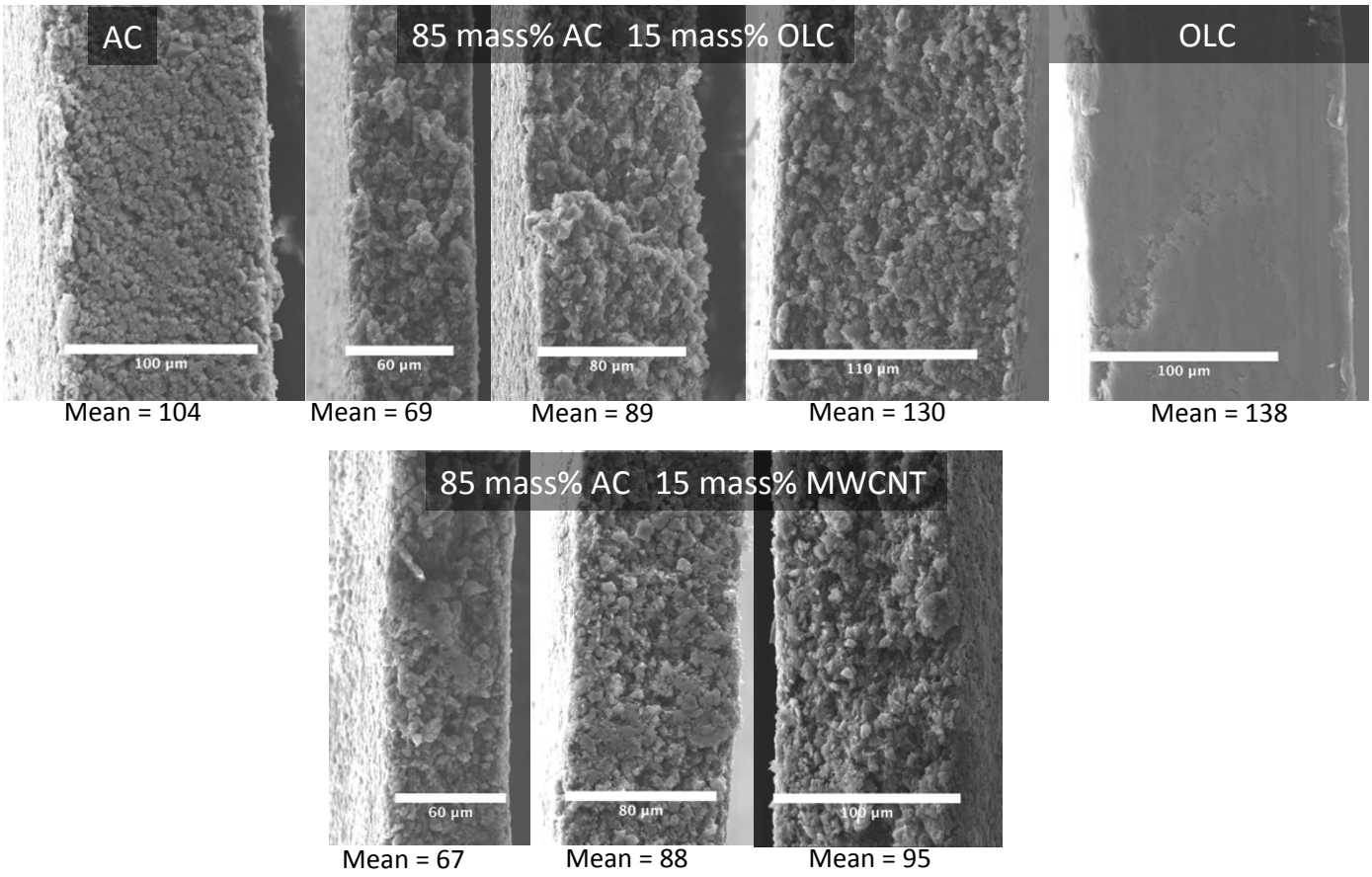

Figure B.6: Scanning electron microscopy (SEM) cross-sectional micrographs of the electrodes.